Dalton Transactions

Accepted Manuscript

ROYAL SOCIETY OF CHEMISTRY

www.rsc.org/dalton

Structural and electrochemical analysis of novel co-electrodeposited Mn_2O_3-Au nanocomposite thin film

[1,2]S. K. Jana*†, [1]B. Saha†, [1]B. Satpati, [1]S. Banerjee

[1]Surface Physics and Materials Science Division, Saha Institute of Nuclear Physics, 1/AF Bidhannagar, Saltlake, Kolkata: 700064, India
[2]Indian Institute of Science Education and Research Kolkata, Mohanpur - 741 246, West Bengal, India

Abstract

In this work we report the fabrication of both pristine Mn_2O_3 and Mn_2O_3-Au composite thin film on indium tin oxide (ITO) substrate by one step novel co-electrodeposition technique. From the electron microscopy study, we observed that these two films are morphologically different. The main aim of this study is to understand the effect of nanostructure and metal integration on the electrochemical charge storage property of these two films. Since charge storage mechanism is possible through faradic red-ox reaction and non-faradic double layer process, so electrochemical characterization and frequency response analysis indicates better charge storage property of the composite system over pristine Mn_2O_3. Mott-Schottky analysis is used for charge carrier estimation which provides the electronic property of both the samples. Besides the mechanism of co-electrodeposition technique, we also discuss in detail the material characterizations on both the pristine Mn_2O_3 and Mn_2O_3-Au composite sample using XRD, EELS and electron microscopy analysis. To the best of our knowledge, the electrochemical property of Mn_2O_3-Au composite sample is reported for the first time.

*E-mail: skj_ec@yahoo.co.on

Keywords: Co-electrodeposition, Mn_2O_3, nanocomposite, electrochemical measurements, EELS

Introduction

Energy storage has been attracted wide interest because of increasing demand of power and energy in the modern electronic devices and electric vehicles. Among various electrochemical energy storage systems, supercapacitors (SCs) have been considered as potential candidates for energy storage because of their higher power density and longer cycle stability than batteries. Enormous efforts are being put to improve the energy/power density of energy storage systems by introducing thin film architectures to electrode materials. The main advantages of the thin film based electrode materials are low ion diffusion length and reduced electron transfer resistance which are related to the major properties of the next generation energy storage systems [1-4]. However, the development of thin film electrodes those capable of storing more energy per unit area has become an urgent issue in order to meet future demands of the electronic industry. Until now, different electrode materials have been widely reported for SCs applications. Mostly those are the based on bulk materials which are carbon based materials [5-6], metal oxides [7-8] and conducting polymers [9]. Transition metal oxides are very attractive materials for charge storage devices because of their ability to store charge by both faradic and non-faradic process [10]. Charge storage in a faradic process can take place either on a surface, as in pseudocapacitors, or in the bulk of the material, as in conventional batteries [11-12]. Non-faradic process dominates in electric double-layer capacitors, in which charge is stored electrostatically from the reversible adsorption of ions onto high surface area of materials [10, 12].

Among the different transition metal oxides, manganese oxide (MnO_2) is one of the good candidates acting as an electrode material for both double layer capacitance and pseudocapcitance [7, 9]. Also, MnO_2 based materials are the most promising for SCs application because of its low cost, high abundance, large theoretical specific capacitance (C_{sp}) and are environmental-friendly. The high capacitance of this material is attributed to the fast and reversible faradaic reaction occurred at the surface. But manganese (II, III, IV etc) oxides have poor electronic property (10^{-5}–10^{-6} S/cm) that limits the high power performance and still remains a major challenge. Since Mn ions have different oxidation states (II, III, IV etc), so there is high chance to obtain any

compound (MnO_2, Mn_2O_3, Mn_3O_4 etc) by slight change of the synthesis condition. In our previous work [7], we performed room temperature electrodeposition on stainless steel for the fabrication of manganese (IV) oxide for supercapacitor application. To improve the electrical conductivity of MnO_2 based electrode material, considerable research efforts have been put for the development of composite materials based on MnO_2 coupled with various conducting materials such as SnO_2 [13], conducting polymers [14-15], graphene [16], carbon nanotubes (CNTs), and carbon [17-18] etc. Also, Park et al [19] shows enhanced specific capacitance of thin film MnO_2 based electrode hybridized with an agarose gel (an ion-permeable and elastic layer coated on current collector). However, no such article has been found yet based on co-electrodeposited Mn_2O_3 along with any material and also on its charge storage application. Here our aim is to fabricate the manganese (III) oxide (Mn_2O_3) on ITO and as the managanese oxide have poor electronic property, so the ultimate goal is to incorporate the conducting metal nanostructure inside the Mn_2O_3 for the investigation of change in electronic property of this functional composite sample. Also it is important to study the effect of metal nanostructure inside Mn_2O_3 on the charge storage property of the composite sample. Therefore both electronic and ionic transport properties as well as the charge transfer reaction at the electrode/electrolyte interface are required for better understanding of electrochemical behaviors, since they govern the charge storage application.

In this work, we developed for the first time Mn_2O_3–Au composite thin-film material by simple one step novel co-electrodeposition technique and both pristine Mn_2O_3 and Mn_2O_3-Au have been fabricated on ITO coated glass substrate for comparative study. In both cases, same pH (~7) of the electrolyte has maintained during electrodeposition. Detailed characterization techniques have been illustrated for the as prepared co-electrodeposited film. The main advantage of the co-electrodeposition of these two materials doesn't require any binder or conductive additives. Structural and morphological changes of both samples were observed microscopically by scanning electron microscopy (SEM) and transmission electron microscopy (TEM) techniques. Electron energy loss spectroscopy (EELS) of the samples was performed to identify the oxidation state of Mn ions. The effects of metal integration on morphology and electrochemical properties of composite Mn_2O_3-Au samples were investigated.

Electronic and ionic properties of the active electrode materials were characterized by both Mott-Schottky (M-S) and electrochemical impedance spectroscopy (EIS) techniques. Charge carrier concentrations in both the samples were obtained by Mott-Schottky analysis. Cyclic voltammogram (CV) on both samples was carried out in order to study the effect of Au nanostructure for enhanced pseudocapacitive charge storage property of the composite sample. Moreover, frequency behavior of both the samples was also studied in order to understand the supercapacitance property of the samples for future charge storage application.

Experimental

Both pristine and composite samples were electrochemically deposited on indium tin oxide (ITO) coated glass substrate controlled by CHI 660C electrochemical workstation (CH Instruments, Inc.) with three electrode configuration adopted with Ag/AgCl as the reference electrode, Pt wire as counter electrode and ITO as working electrode. Prior to deposition all ITO substrates were cleaned ultrasonically with acetone and ethanol for half an hour followed by rinse with de-ionized (DI) water (20MΩ-cm). Both pristine and Mn_2O_3-Au composite films were grown on ITO substrates using cyclic voltammetry technique with scan rate of 0.06 V/s for 4 cycles within potential range between -1.2 to 1V maintaining the electrochemical cell temperature at 50^oC. Pristine Mn_2O_3 was deposited using aqueous 0.1M manganese acetate ($Mn(CH_3COO)_2$) and 0.1M sodium sulfate (Na_2SO_4) solution while Mn_2O_3-Au was grown by adding of 0.001M chloroauric acid ($HAuCl_4$) to the above electrolyte mixture. Same pH (~7) of the mixed electrolyte and same growth condition was maintained during the preparation of both pristine and composite Mn_2O_3 sample. However, all the chemicals (99.9% pure) required were purchased from Merck India Chemicals Pvt. Ltd.

The surface morphology of both pristine and Mn_2O_3-Au composite was obtained from SEM measurement carried out using FEI and detailed structural information was carried out using transmission electron microscopy (TEM) TF30, ST microscope operating at 300 kV. The TEM is equipped with a scanning unit and a high angle annular dark-field (HAADF) detector from Fischione (model: 3000). Electron energy loss spectroscopy (EELS) was carried out using a post column Gatan Quantum SE (model:

963 SE) in the same microscope. The samples were mounted on a carbon coated Cu grid, and used for TEM measurements. EELS spectra of both the Mn_2O_3 and Mn_2O_3-Au were obtained from different position of the sample using high angle annular dark-field scanning transmission electron microscopy (STEM-HAADF) mode with probe size of ~1nm. Crystal structure of both the samples was characterized by X-ray Diffraction (XRD) instrument (Bruker AXS D8). All the electrochemical characterizations were performed in room temperature using 0.1M Na_2SO_4 electrolyte with three electrode configuration.

1. Results and discussions:

(a) Mechanism of co-electrodeposition technique of both Mn_2O_3 and Mn_2O_3-Au

The mechanism of composite formation through co-electrodeposition technique is discussed elaborately in Fig. 1 &. 2 shown bellow.

(i) *Mn_2O_3 formation mechanism*

Fig. 1 shows the typical CV curves of both Mn_2O_3 and Mn_2O_3-Au, electrodeposited on ITO. Fig. 1a shows the repetitive CV curves (4 cycles) of the deposition process of pristine Mn_2O_3 on the ITO surface immersed in electrolyte mixture (pH~7) containing aqueous Na_2SO_4 and $Mn(CH_3COO)_2$. The two anodic peaks ($P1_a$, $P2_a$) in Fig. 1a are attributed to the oxidation of Mn^{2+} to Mn^{3+} and Mn^{3+} to $Mn(OH)_3$. With the increase of scan number, slowly raised of two oxidation peaks indicates the formation of Mn_2O_3 film. The details reactions involved in Mn_2O_3 formation can be proposed through electron transfer - chemical reaction - electron transfer (ECE) mechanism as expressed in equations (1)-(6). Similar ECE mechanism was reported in case of MnO_2 formation [20].

Both deposition (oxidation) and reduction of Mn_2O_3 through ECE mechanism

$$Mn^{2+} \rightarrow Mn^{3+} + e^- \quad (1) \ldots\ldots \text{peak } P1_a$$

$$Mn^{3+} + 3H_2O \rightarrow Mn(OH)_3 + 3H^+ + 3e^- \quad (2) \ldots\ldots \text{peak } P2_a$$

$$2Mn(OH)_3 \rightarrow Mn_2O_3 + 3H_2O \quad (3)$$

The cathodic peak in the $P3_a$ region may be due to the reduction of $Mn(OH)_3$, which is further reduced to Mn^{2+} in the $P4_a$ potential region.

$$Mn_2O_3 + 3H_2O \rightarrow 2Mn(OH)_3 \quad (4)$$

$$Mn(OH)_3 + 3H^+ + 3e^- \rightarrow Mn^{3+} + 3H_2O \quad (5) \ldots\ldots \text{peak } P3_a$$

$$Mn^{3+} + e^- \rightarrow Mn^{2+} \quad (6) \ldots\ldots \text{peak } P4_a$$

From equations (1)-(6), it is observed that deposition process of pristine Mn_2O_3 is completely vice versa of reduction mechanism, only difference is that deposition or anodic oxidation current is higher than the cathodic reduction current. This means the deposition process is anodic and is dominant than the cathodic reduction mechanism.

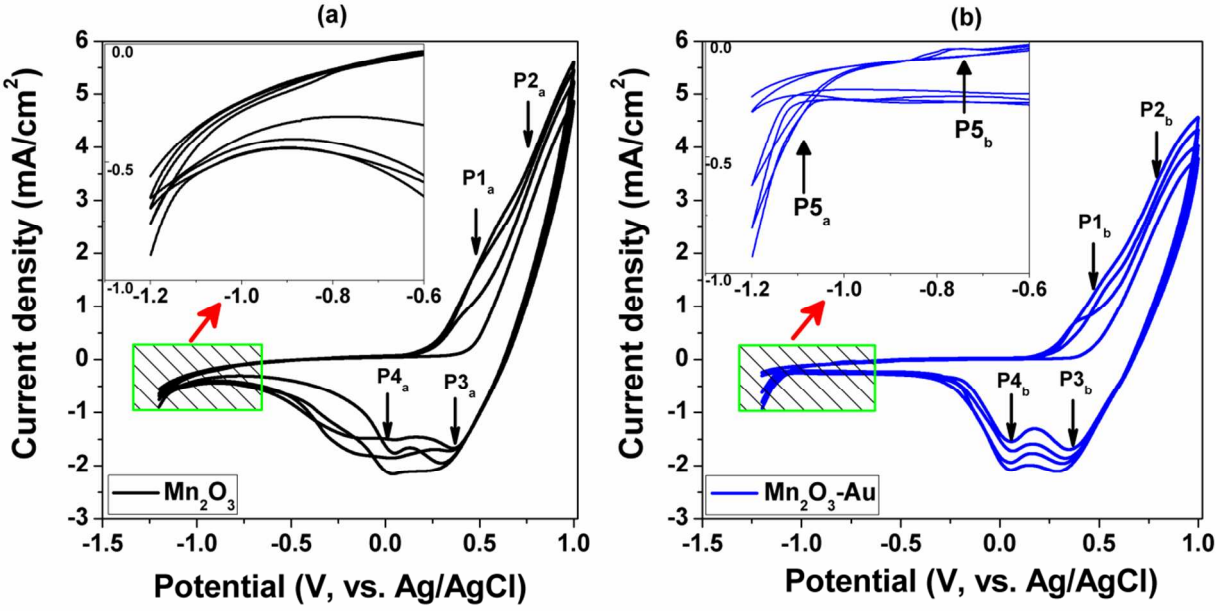

Fig. 1: Comparative CV graphs for the electrodeposition of both (a) Mn_2O_3 and (b) Mn_2O_3-Au

(ii) ***Mn_2O_3-Au formation mechanism***

Fig. 1b shows the CV curve of co-electrodeposited Mn_2O_3-Au samples grown in same pH (~7) of the electrolyte. Compared to Fig. 1a (pristine Mn_2O_3), we observe an extra oxidation peak ($P5_b$ at ~ -0.8V) in Fig. 1b and consequently a clear current density increase is seen around -1.1 V, proving the cathodic deposition of Au into Mn_2O_3 matrix. Rate of deposition can be observed by the increasing red-ox peaks with number of sweeps. Increasing tendency of the reduction peaks ($P6_b$) with number of cycles indicate increasing gold concentration inside the Mn_2O_3 matrix. Reduction (cathodic

deposition of Au) peak potential of Au is consistent with our previous report on gold electrodeposition [21].

The mechanism of Au formation from $AuCl_4^-$ is involved in the cathodic cycle. In the cathodic cycle, reduction of Mn_2O_3 to MnOOH occurs first according to equation (7) followed by reduction of $AuCl_4^-$ to Au as expressed in equation (7). The reaction mechanism can be expressed as following.

$$AuCl_4^- + 3e^- \rightarrow Au + 4Cl^- \qquad (7) \ldots\ldots \text{peak } P6_b$$

The whole reaction mechanism involved with Mn_2O_3-Au formation can be represented schematically in Fig. 2. In step 1, Mn^{2+} ions adsorbed at the ITO surface and in step 2 Mn^{2+} converts to Mn^{3+} at ~ 0.5V. Finally it oxidized at ~1V and forms Mn_2O_3 as described in equations (1)-(3). In step 3, some of the as formed Mn_2O_3 gets reduced and is converted to unstable Mn^{2+} which is mentioned in equations (4)-(6). Step 4 and step 5 describes the Au nucleation starts at oxidation cycle and is cathodically deposited in the reduction cycle same as equation (7).

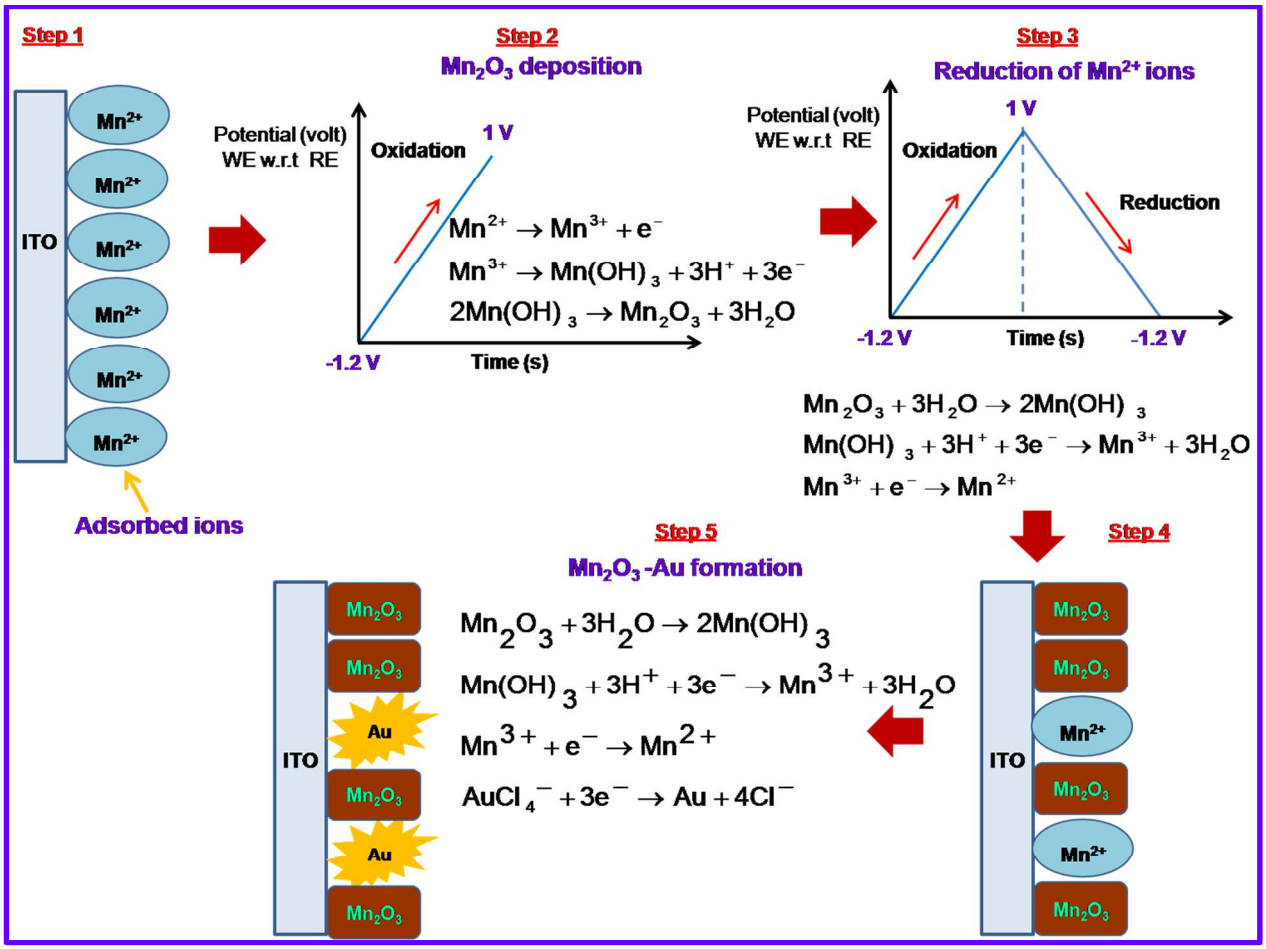

Fig. 2: Schematic representation of co-deposition mechanism of Mn_2O_3–Au on ITO.

(b) ***Microscopical analysis***

Fig. 3a and 3b show the scanning electron microscopy (SEM) images of both pristine Mn_2O_3 and Mn_2O_3-Au samples grown in same pH of the electrolyte. It can be seen from SEM images that the morphology of both the samples is different from another. From Fig. 3a we can say that the Mn_2O_3 film has smooth wrinkles whereas, rough wrinkles and more porous film is observed in Fig. 3b for the Mn_2O_3-Au sample. From the

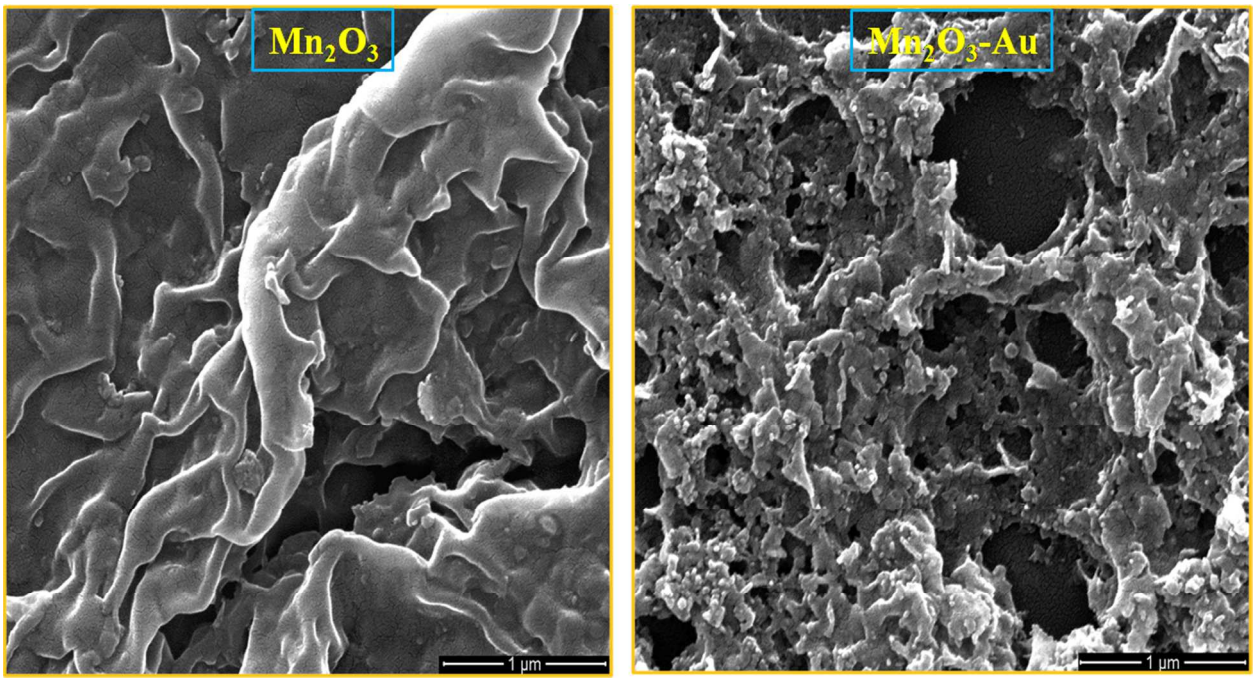

Fig. 3: SEM image of (a) Mn_2O_3 (b) Mn_2O_3-Au composite sample

secondary electron image (Fig. 3b) it was hard to find any evidence of Au on the surface Mn_2O_3. The probable reason of this might be the embedded of Au inside the Mn_2O_3 matrix. So detail morphological, structural and crystalline information of the samples were analyzed using transmission electron microscopy (TEM). Spectroscopic analysis of the samples was also done by EELS measurements in the TEM. Fig. 4a-4c and Fig. 5a-5e represent the TEM analysis of as prepared pristine Mn_2O_3 and Mn_2O_3-Au composite sample respectively. Fig. 4a is the TEM image and Fig. 4b represents STEM-HAADF image of Mn_2O_3. Electron diffraction pattern of pristine Mn_2O_3 is shown in the inset of Fig. 4a which shows the presence of nano crystallites and the diffraction planes of the sample are indexed on SAED pattern (see inset). Indeed in the high-resolution TEM image of Fig. 4c shows such crystallites besides the presence of high rippling and the edge of ripple can also be observed in the HRTEM image. Fig. 5a corresponds to the TEM image of Mn_2O_3-Au composite sample. It is clearly observed that urchin like gold nanostructure embedded in Mn_2O_3 matrix. EDX spectrum from area '1' of the STEM-HAADF image of Fig. 5b is shown in Fig. 5c confirms the elemental composition of the same sample. Cu and C signal in EDX spectrum is due to carbon coated Cu grid

used for TEM study. Chemical mapping using STEM-HAADF-EDX technique of individual component of Mn_2O_3-Au composite sample from area 2 (see Fig. 5b) is shown in the Fig. 5d.

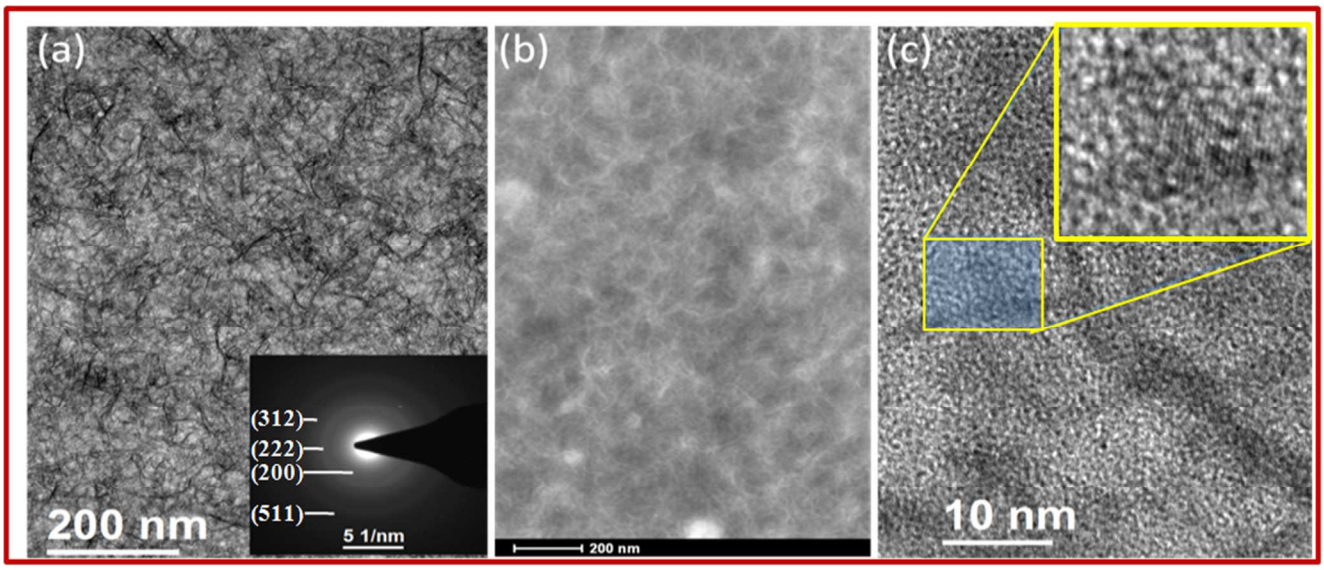

Fig. 4: (a) Bright-field TEM image, (b) STEM-HAADF image (c) HRTEM image of Mn_2O_3 sample and in the inset showing nanocrystals.

Both electron diffraction pattern and HRTEM image of individual Mn_2O_3 matrix (marked with red dotted circle '1') and Au with Mn_2O_3 (marked with red dotted circle '2') is depicted in Fig. 5e. HRTEM of Mn_2O_3 matrix confirms the crystals are formed and well defined electron diffraction pattern is ascribed. Same observation is also found in case Au nanostructured embedded in Mn_2O_3. Both electron diffraction pattern and HRTEM image of individual Mn_2O_3 matrix (marked with red dotted circle '1') and Au with Mn_2O_3 (marked with red dotted circle '2') is depicted in Fig. 5e. HRTEM of Mn_2O_3 matrix confirms the crystals are formed and well defined electron diffraction pattern is ascribed. Same observation is also found in case Au nanostructured embedded in Mn_2O_3. The diffraction spots can be indexed as (200), (222), (312) and (511) reflections of cubic α-Mn_2O_3 (JCPDS 71-0635) from dotted circle '1' whereas diffraction spots can be indexed as (200), (122), (222), and (312) reflections of cubic α-Mn_2O_3 (JCPDS 71-0635) from dotted circle '2' with Au (111) spot. The HRTEM images indeed show the presence of such nanocrystals. The inter planer spacing (d-spacing) 4.71 Å in Fig. 5(e)- ii could be

(200) of α-Mn_2O_3 and d-spacing of 2.31 Å in Fig. 5(e)- iii could be (111) of Au (d_{200} for α-Mn_2O_3 is 4.70 Å and d_{111} for Au is 2.35 Å.).

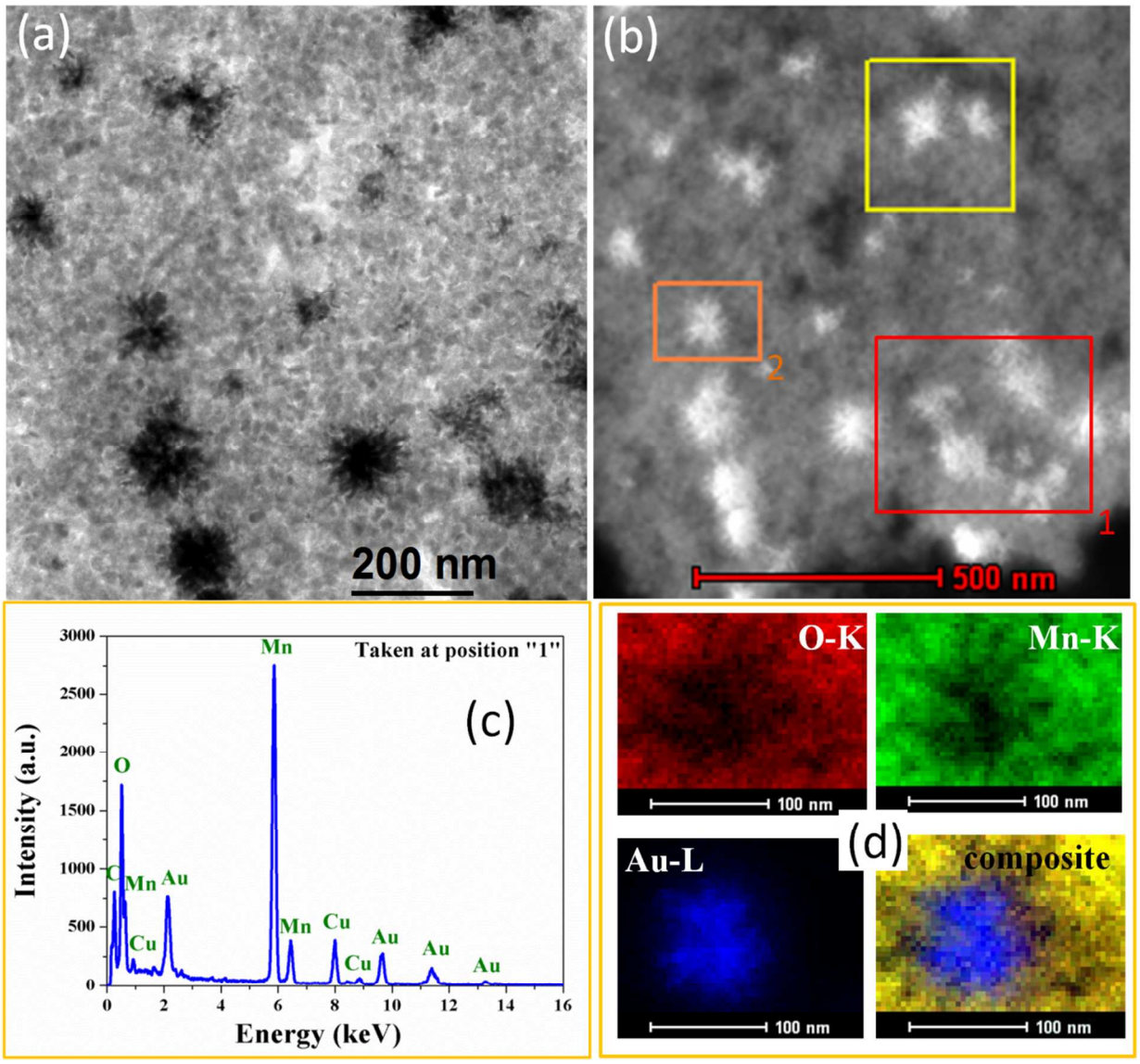

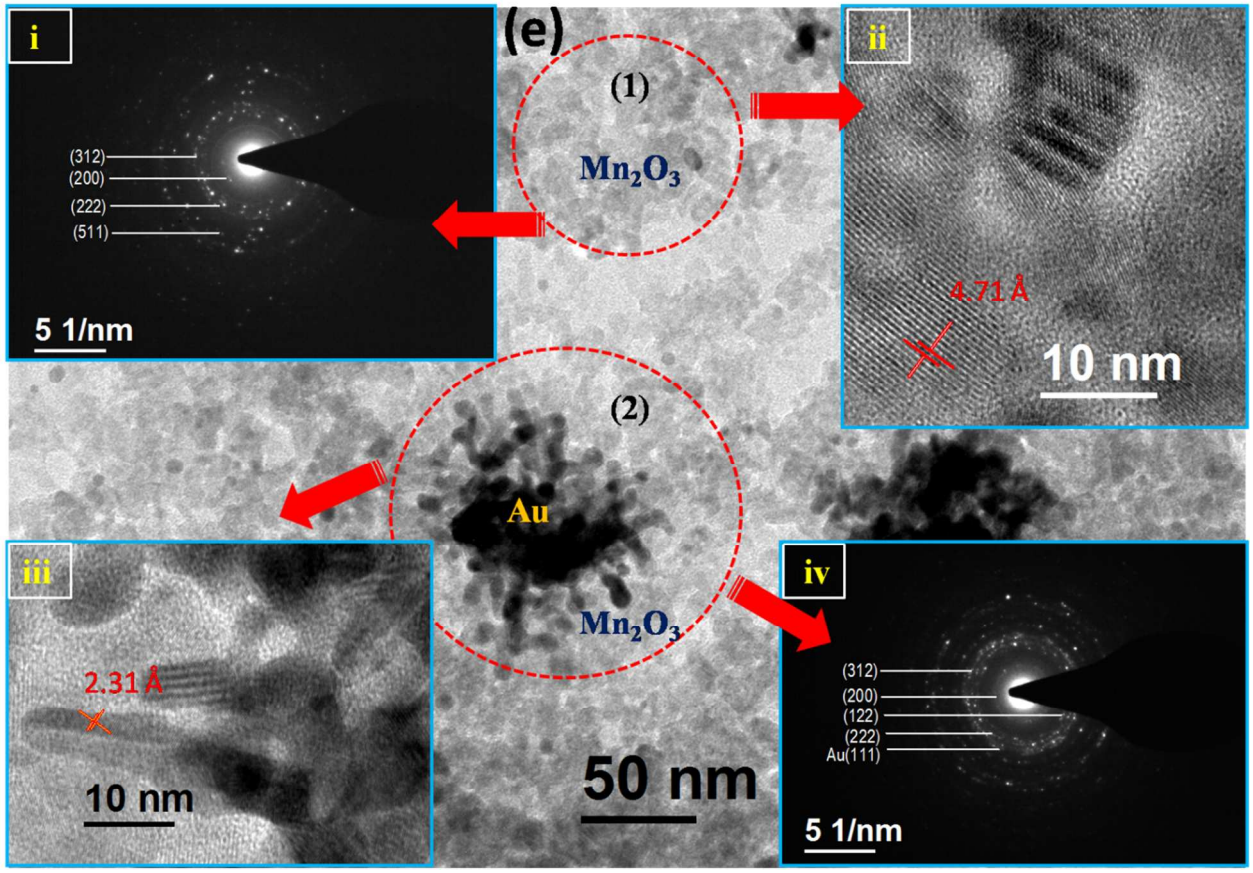

Fig. 5: (a) TEM image (b) STEM-HAADF image, (c) EDX spectrum, (d) Elemental mapping, and (e) SAD and HRTEM images from different area of Mn_2O_3-Au composite sample.

(c) Structure and chemistry of both pristine Mn_2O_3 and Mn_2O_3-Au composite

(i) XRD analysis

XRD analysis of the as deposited samples (both pristine Mn_2O_3 and Mn_2O_3-Au composite) including bare ITO is shown in the Fig. 6. Though both the samples are thin film (thickness~400 nm), the corresponding diffraction peak of the materials itself is not so prominent. A small peak around $2\theta \sim 33^{o}$ (encircled with dotted rectangular region) is attributed to the main characteristic feature of [222] plane of Mn_2O_3 phase of the sample. The same feature has also been reported in the recently published article by A. Ramírez et al. [22]. Both pristine and composite sample were grown in the same phase as confirmed by the [222] plane of XRD analysis. This phase is also consistent with the EELS analysis which is shown in Fig. 7.

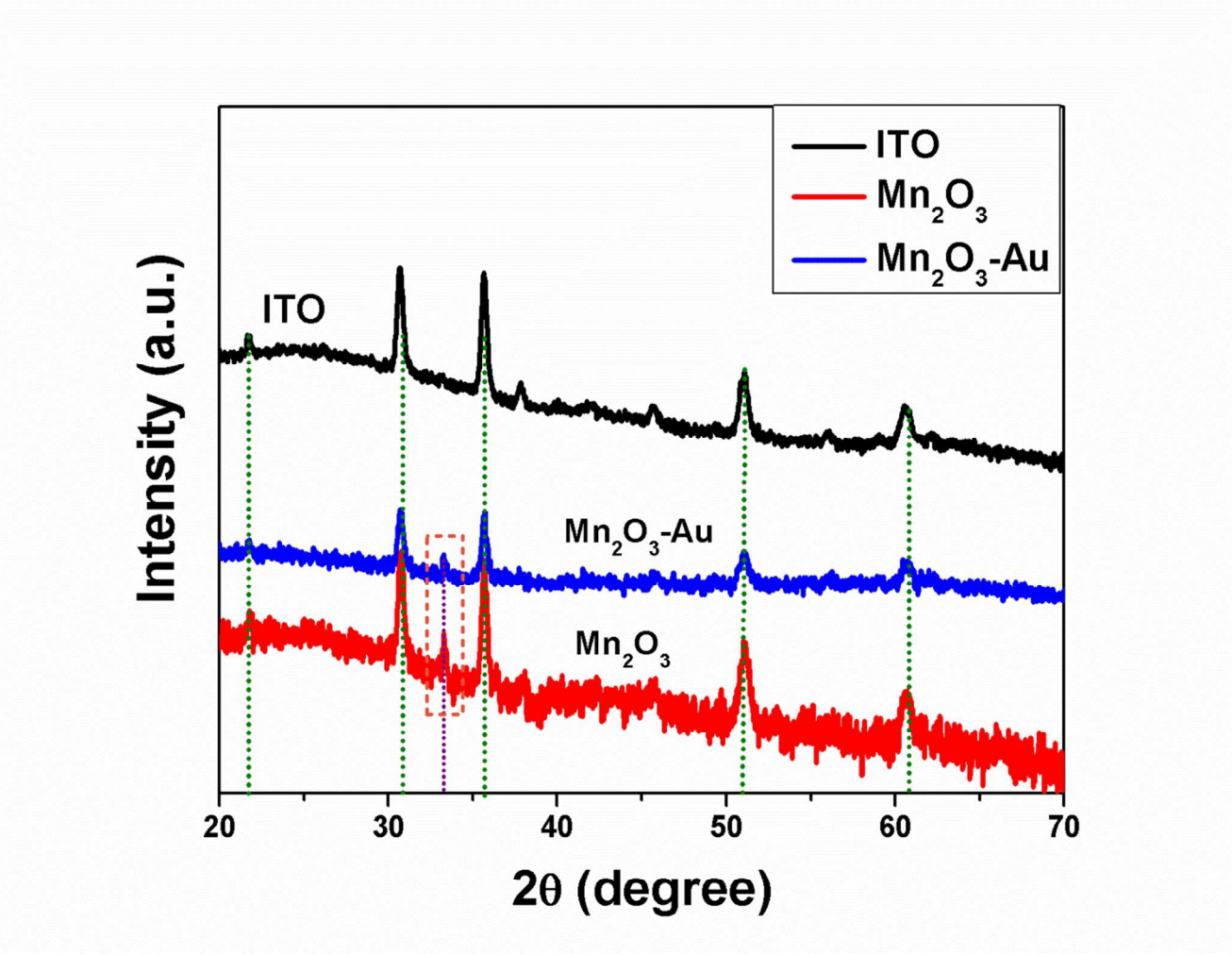

Fig. 6: XRD analysis of both pristine Mn_2O_3 and Mn_2O_3-Au composite sample.

(ii) EELS analysis:

Electron energy-loss spectroscopy (EELS) in a transmission electron microscope has been widely used to determine the oxidation state. EEL spectra of the pristine Mn_2O_3 from different points (probe size ~ 1nm) on the sample surface are shown in Fig. 7a.

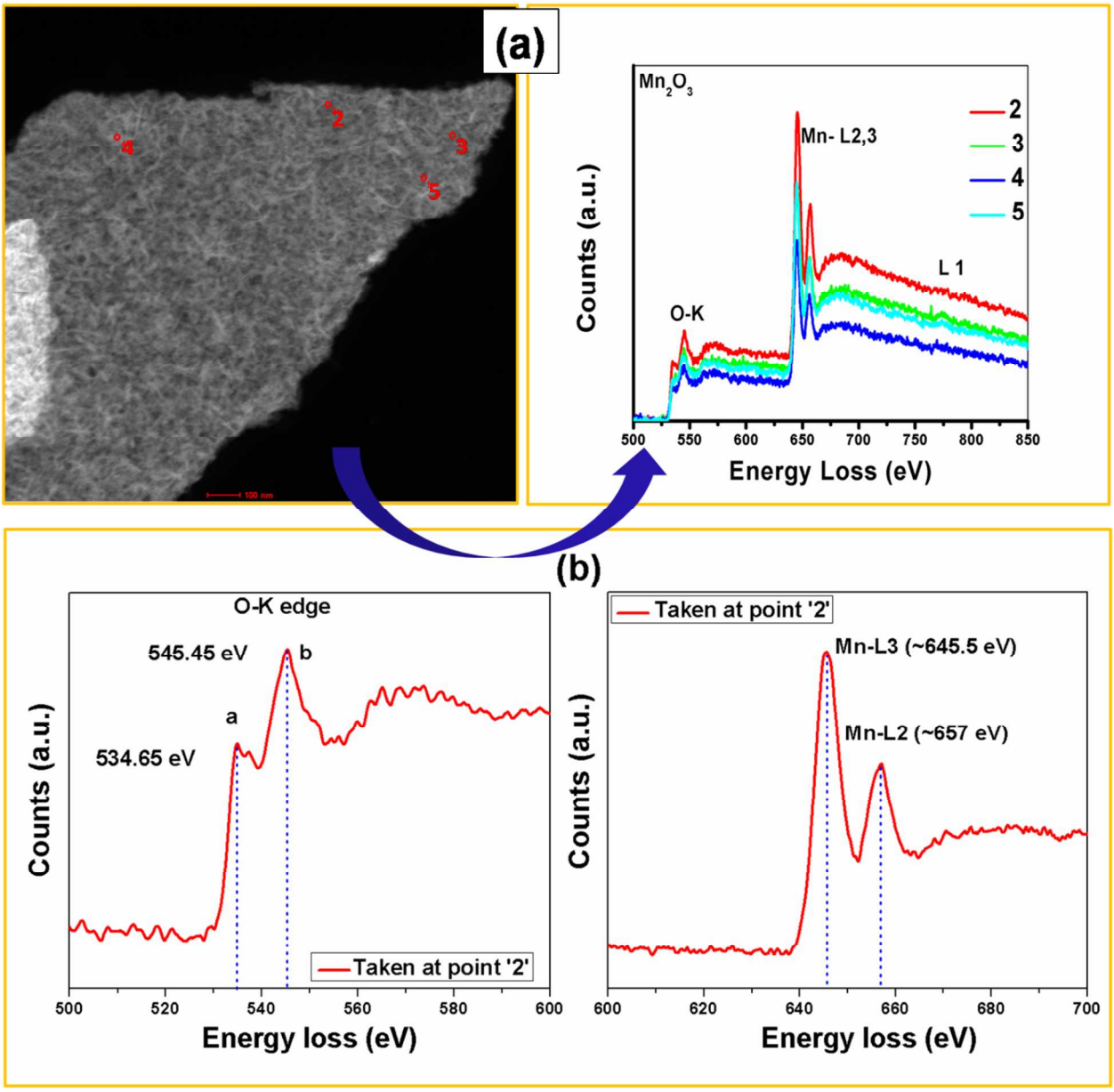

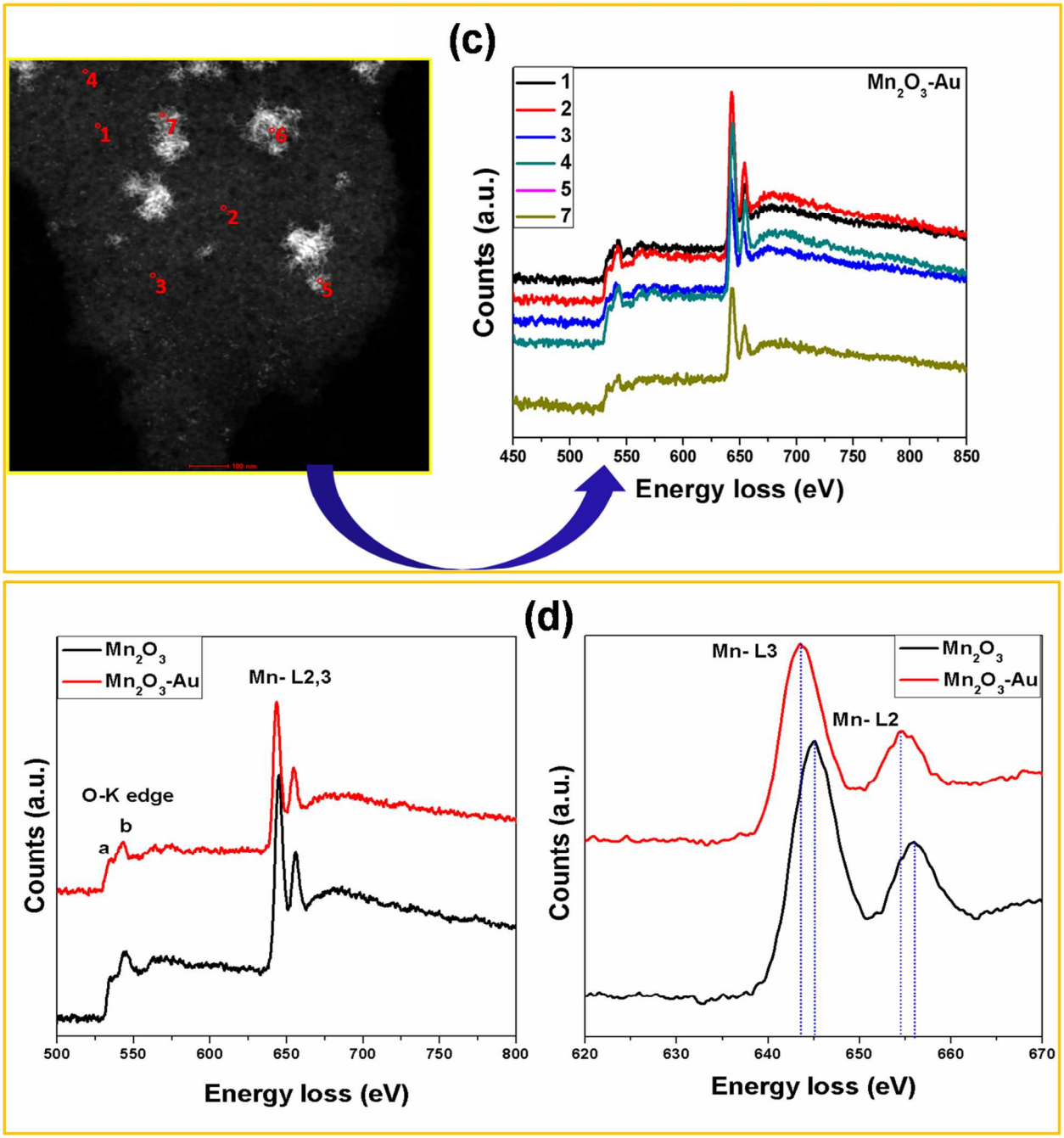

Fig. 7: (a) HAADF image (left) and corresponding EELS spectra of pristine Mn_2O_3 at different probe points **(b)** separate O-K edge and Mn $L_{2,3}$ graph of EELS of single probe point '2' **(c)** HAADF image (left) and corresponding EELS spectra of at different probe points Mn_2O_3-Au and (d) Comparative analysis of EELS spectra of both pristine Mn_2O_3 and Mn_2O_3-Au (left) and Mn-L2,3 edges (right).

Spectra from different points indicate that the pristine sample is grown with same phase all over the surface. EEL spectra were collected from 400 to 920 eV region using energy dispersion of 0.1 eV. Spectrum from this region shows two distinguished edges one for Mn-$L_{2,3}$ edge (640 eV) and other for O-K edge (532 eV) gives us information on transition of oxygen 1s electrons to 2p bands, which are oxidized with empty Mn 3d orbital. Separate plot of both Mn-$L_{2,3}$ and O-K edge is shown in Fig. 7b. The sharp edge of Mn-$L_{2,3}$ consists of two peaks related to the electron transitions from $2p_{3/2}$ (L_3 edge) and $2p_{1/2}$ (L_2 edge) core states to the unoccupied 3d states. The position of the oxygen K and manganese $L_{2,3}$ edges and the intensity ratio of "white-lines" (WL) [23] $I(L_3)/I(L_2)$, are characteristics of determination of the oxidation state of manganese [23]. The two main characteristic peaks of oxygen K edge can be described in terms of transition processes governed by the dipole selection rule. The peak 'a' around 535 eV has been ascribed due to the electron transition from the 1*s* oxygen core state to the 2*p* state hybridized with manganese 3*d* orbital [24]. The second peak 'b' is related to the probable unoccupied oxygen 2p states mixed with the manganese 4sp. The position (at ~535 eV) of peak 'a' in the EELS spectra corresponds to the Mn_2O_3 phase of the material. This result is also consistent with earlier reports [23-24]. The energy separation between the peak 'a' and peak 'b' of is ~10.8 eV which also confirms the Mn_2O_3 phase [23]. To find out WL intensity ratio $I(L_3)/I(L_2)$ there are many methods which have been already reported [25]. Among these, Pearson method [26] is more popular and accurate method to extract the WL ratio. According to Pearson model, the experimental edge difference region is approximated by two steps functions in the Mn-L edge i.e. the energy difference between Mn-L_3 and Mn-L_2. The detail extraction method is described in the references [23, 26]. Using Pearson extraction method we obtained the WL ratio of our sample is about 2.35 to 2.4 (depending upon fitting accuracy) which exactly matches with earlier reported value ~2.44 [23] and 2.32 [27].

EELS spectra of Mn_2O_3-Au sample at different probe points (numbered in red color on the HAADF image of the same sample) are also shown in Fig. 7c. The probe points were on both Au nanostructures as well as on the Mn_2O_3 matrix. The EELS spectrum taken at all probe points on Mn_2O_3 is almost indifferent constituting the same phase of the material, while the shift of Mn-L2,3 peaks towards lower energy losses was

observed in case of Mn_2O_3-Au, Fig. 7d so we can conclude that there is a bond formation between Mn_2O_3 and Au. These results manifest the changes in bonding structure and electronic properties of the conjugated thin films, implying the formation of hetero-structured Mn_2O_3-Au thin film.

(d) Electrochemical measurements

(i) Mott-Schottky analysis

To investigate the mechanism for the enhanced electrical conductivity of Mn_2O_3-Au, Mott-Schottky (MS) measurements were conducted. This method was based on the Schottky barrier formation between the semiconductor material and an electrolyte [26]. The variation of the space charge capacitance (C_{sc}) was measured as a function of the applied potential. As shown in Fig. 8, both Mn_2O_3 and Mn_2O_3-Au samples exhibit a positive slope, indicating n-type semiconductor character. Carrier densities (N_d) of the samples were calculated using the following equation [28-29].

$$N_d = \frac{2}{\varepsilon\varepsilon_0 e A^2} * \frac{dV}{dC_{sc}^{-2}} \qquad (8)$$

Where, ε is the relative dielectric constant of Mn_2O_3 (~1.5×10^4) [30], ε_0 is the permittivity of vacuum, V is the potential applied at the electrode, and A is the area of the electrode material. The ratio of the carrier densities of both the samples was calculated from equation 8 (with A_{Mn2O3}~0.4 cm^2 and $A_{Mn2O3\text{-}Au}$ ~0.36 cm^2 and same ε of both the samples) and it is inversely proportional to the slope of the MS plot of both samples. From this calculation we have found that carrier density of Mn_2O_3-Au is 3.7 times higher than the carrier density of pristine Mn_2O_3 sample. Also the carrier densities of both pristine and composite samples were calculated to be 2.1×10^{14} and 7.8×10^{14} cm^{-3} respectively. In Mn_2O_3-Au composite films, Au is the source of extra charge carriers. In Fig. 8, we observe that MS plot of Mn_2O_3-Au having lower slope represents the higher carrier concentration compared to pristine Mn_2O_3. Higher charge carrier concentration in the composite sample has an influence to change the work function of the material. This has an effect on more band bending which enhances the charge transfer at the electrode electrolyte interface (shown in Fig. 9).

Electrochemical impedance spectroscopy (EIS) was conducted to understand the conductivity of electrode material, charge transport in the electrode-electrolyte interface and mechanistic analysis of interfacial processes. Fig. 9a shows the Nyquist plot of both pristine Mn_2O_3 and Mn_2O_3-Au composite samples. These two plots display a semicircle in the high

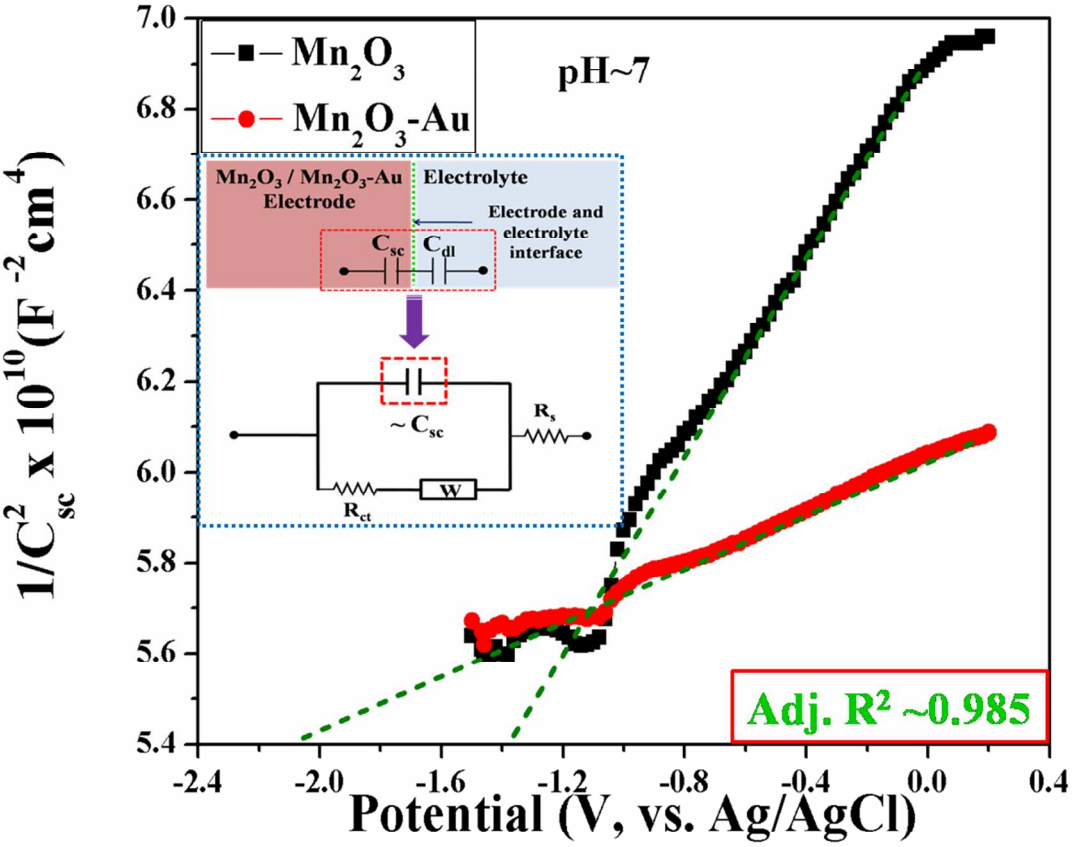

Fig. 8: Mott- Schottky plot of both pristine Mn_2O_3 and Mn_2O_3-Au. Inset schematic shows proposed Randle's circuit where capacitance is replaced by space charge capacitance (C_{sc}). Because both C_{sc} and double layer capacitance (C_{dl}, which is large than C_{sc}) are in series. So equivalent capacitance is C_{sc}. R_{ct}, W, and R_s are the charge transfer resistance, Warburg impedance and series resistance of the device respectively.

frequency region and a straight line in the low-frequency region, which corresponds to electron-transfer-limited and diffusion-limited electron transfer processes, respectively.

Inset graph shows the Nyquist plot of both the sample at frequency range from 100 KHz to few Hz. There are two intercepts of the semicircle to real impedance axis at the high frequency region. At very high frequencies (~100 KHz), the intercept at real part (marked with blue arrow in the inset graph of Fig. 9a) is a combination resistance of ionic resistance of electrolyte, and contact resistance at the active material/current collector interface [31]. These two intercepts show the two different values (~18 Ω for Mn_2O_3 and ~7.3 Ω for Mn_2O_3-Au). Decrease of this resistance value is attributed to the improvement of current collector resistance (in both cases solution resistance is the same for same solution) property of Mn_2O_3-Au sample because of Au improves the interfacial resistance between current collector (ITO) and active material (Mn_2O_3-Au). Another major difference in the Nyquist plots is the arc of the semicircle in the high frequency range (marked with pink color arrow in the inset graph of Fig. 9a), which corresponds to the charge-transfer resistance (R_{ct}) which is associated with the electronic properties of porous electrode. The R_{ct} of Mn_2O_3-Au is (~30Ω) much lower than R_{ct} of Mn_2O_3 (~130Ω). Decrease of charge transfer resistance of Mn_2O_3-Au is ascribed due to large number of charge carriers in bulk of the same sample. These charge carriers is only because of presence of Au inside the Mn_2O_3 which facilitate fastest electron transport and shortest ion-diffusion path inside the Mn_2O_3-Au. Another feature of the Nyquist plots is the straight line in the low frequency range (10 Hz to 10 mHz) which corresponds to the Warburg impedance [32] associated with diffusion of ions inside the porous electrode material. Also this straight line makes an angle (called phase angle) with Z_{real} axis. In our case, we observe that Warburg impedance is lower in Mn_2O_3-Au compared to Mn_2O_3. This result indicates that Mn_2O_3-Au shows better pseudocapacitive nature compared to Mn_2O_3. Moreover, increase in the phase angle (marked with green arrow) which indicates capacitance nature of the active electrode material. Thus, Mn_2O_3-Au shows much ideal capacitance than the Mn_2O_3. This can be illustrated in detail in the frequency dependence phase angle (Bode plot) plot of both Mn_2O_3 and Mn_2O_3-Au sample shown in Fig. 9b.

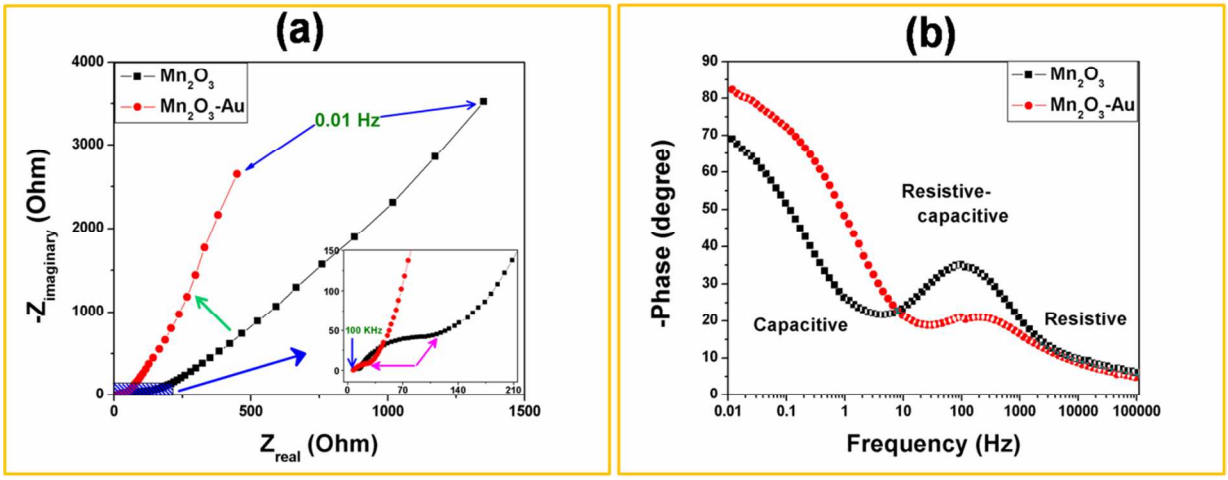

Fig. 9: Comparative study of (a) Nyquist plot and (b) frequency response on change in phase angle (Bode plot) of both Mn_2O_3 and Mn_2O_3-Au sample.

The Bode plot (Fig. 9b) can be separated into high, medium and low frequency regions. At the high frequency region (above ~300 Hz) the phase angle has tendency to be close to zero and the characteristic behavior of the samples in this region is like as a resistor and at low frequency region (below ~1Hz) it indicates capacitive behavior. Approaching the phase angle towards the -90° attributes to the device behavior like an ideal capacitor [33]. In this case Mn_2O_3-Au sample shows more capacitive nature than the pristine Mn_2O_3. The charge transfer resistance at high frequency region is described already in Fig. 9a. Between these two states both the samples behave as R-C transmission line and in our case (above 10 Hz and below 2 KHz) two peaks are associated with the impedance of the R-C transmission line for the two samples. Higher the peak intensity of phase angle of Mn_2O_3 indicates its higher impedance compared to Mn_2O_3-Au and frequency associated with phase angle position of the two samples corresponds to the "Fig. of merit" [33] of the respective samples. Mn_2O_3-Au shows higher "Fig. of merit" pointed out better ac response of the sample compared to Mn_2O_3.

Moreover, frequency analysis of complex capacitance is to describe capacitive nature of the electrode material [32] shown in Fig. 10a and Fig. 10b. In Fig. 10a, C' represents the real part of the capacitance; it shows the variation of the available stored energy with the frequency. As we have described that the majority of the capacitance is

only available at lower frequency, the same characteristics is obtained in both samples. In this case, Mn_2O_3-Au exhibits higher capacitance than pristine Mn_2O_3.

Fig. 10b shows the frequency behavior of the imaginary part of the capacitance (C") which represents the losses that occur during charge storage [32, 34]. This graph presents the capacitive dispersion related to energy losses. The peaks observed for each device can be used to determine the typical frequency attached to the relaxation time τ_0. This defines ions diffusion inside bulk of the electrode material [33] and fast ions diffusion inside the material attributes to the lower τ_0. The curved peaks (marked by downward arrow in Fig. 10b) of the spectrum can be used to determine the relaxation time constant (τ_o) of the two samples. The time constant τ_o is calculated from maximum frequency (f_p) using the equation $\tau_o = 1/f_p$ and the values are 50 and 1s for Mn_2O_3 and Mn_2O_3-Au respectively. It is well known that higher power delivery corresponds to lower τ_o value [34-35] of the same sample. So presence of Au nanostructure improves the supercapacitor power of Mn_2O_3-Au compared to Mn_2O_3.

Fig. 11a shows comparative study of the cyclic voltammograms (CVs) of both bare Mn_2O_3 and Mn_2O_3-Au films at a fixed scan rate of 0.06 Vs^{-1}. In this Fig. we observe that Mn_2O_3-Au reveals highest current compared to pristine Mn_2O_3. The enhancement of current of Mn_2O_3-Au over pristine film is ascribed due to the effect of Au incorporation inside the Mn_2O_3. In Fig. 11a, one can easily distinguish two

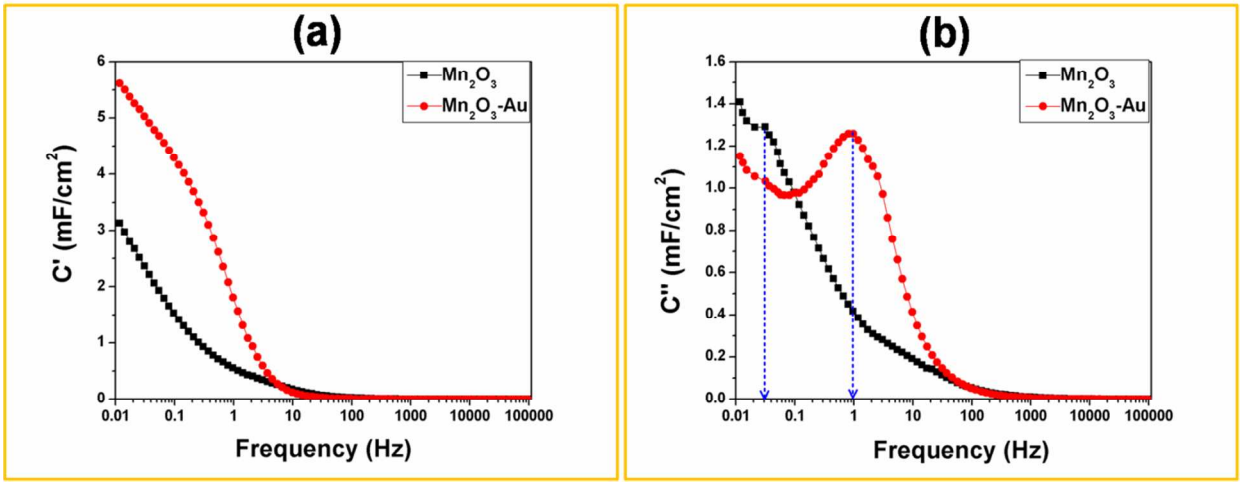

Fig. 10: Analysis on the (a) real part of the capacitance vs. the frequency and (b) imaginary part of the capacitance vs. the frequency of both Mn_2O_3 and Mn_2O_3-Au.

potential regions (0-0.5V and 0.5-1V) where current density of both electrodes is independent and dependent with applied potential respectively. This means both electrodes exhibit double layer capacitance in potential range 0-0.5V where capacitance (dQ/dV) is a constant and independent of voltage. Enhancement of current so as charge storage capacity in this region is obtained due to the increase of overall surface area of Mn_2O_3-Au sample because of hierarchical Au nanostructure inside the Mn_2O_3 matrix. However, due to the low mass loading of our material, reliable BET measurements were not possible because it was difficult to measure the mass of the electrodeposited material. In the potential region 0.5-1V, pseudocapacitance (dQ/dV is voltage dependent) is attributed due to faradic red-ox reaction which is confirmed by the red-ox peak identified by blue arrow in Fig. 11a. The enhancement of pseudocapacitive peak current is much higher than double layer current, so that we can say Au nanostructures not only increase the double layer current but also boost up the faradic current by charge transfer process during red-ox reaction. This faradic charge transfer originates by a very fast sequence of reversible red-ox, electrosorption or intercalation processes. Presence of Au inside the Mn_2O_3 matrix can enhance the Faradic charge intercalation process and hence enhances pseudocapacitance value. Moreover, both pseudocapacitance and double-layer capacitance contribute individually to the total capacitance value of supercapacitor. As expected, the Mn_2O_3-Au composite electrodes exhibited significantly higher charge storage capacity than pristine Mn_2O_3. The charge-storage mechanism of MnO_2 based material is described in the references [7, 36]. The mechanism is based on surface adsorption of electrolyte cations (Na^+) as well as proton incorporation according to the reaction:

$$\mathrm{MnO_2} + \mathrm{xNa^+} + \mathrm{xe^-} \leftrightarrow \mathrm{MnO_2(xNa)} \qquad (9)$$

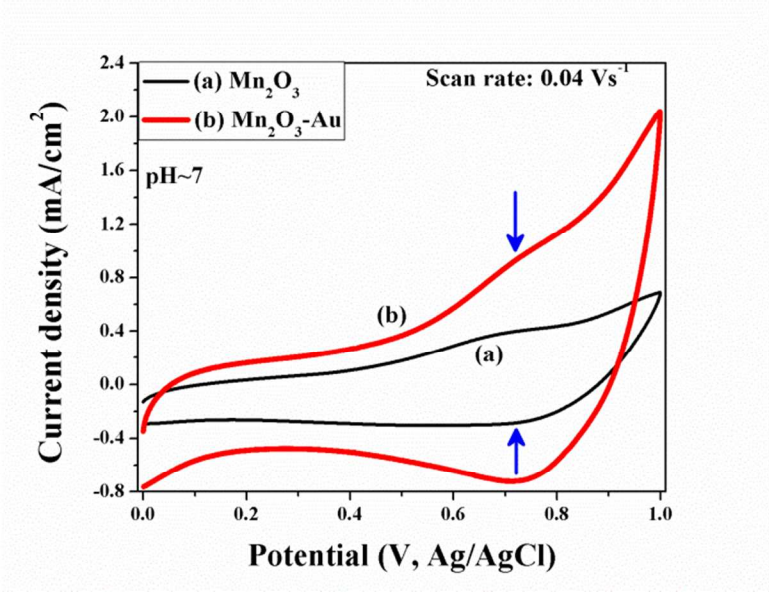

Fig. 11a: CV profile of both pristine and composite sample at a fixed scan rate of $0.04Vs^{-1}$.

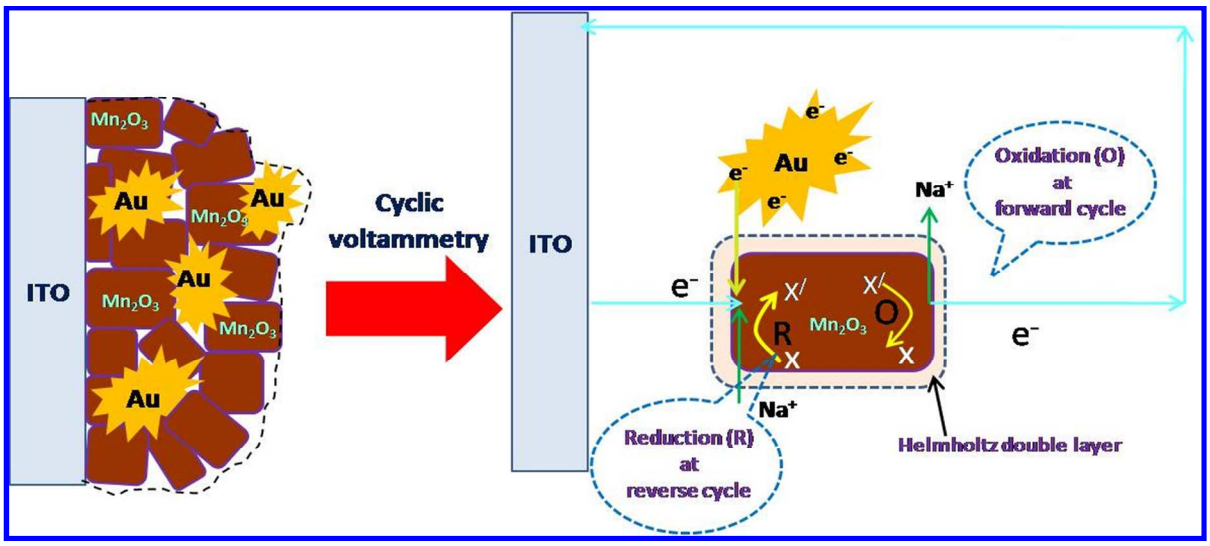

Fig. 11b: Schematic representation of enhanced pseudocapacitive current of Mn_2O_3-Au.

Pseudocapacitance is associated with faradic charge transfer process between Mn_2O_3-Au electrode and electrolyte (Na_2SO_4). The enhancement of pseudocapacitive current is described schematically in Fig. 11b. Au nanostructure have large number of free surface charges which take part in the reversible faradic red-ox reaction process as described in the above equation. Enhancement of pseudocapacitive current is

measured by CV analysis of Mn_2O_3-Au sample. During cathodic potential scan (1V to 0V), electrons from ITO (e^-_{ITO}) and extra surface charge from Au (e^-_{Au}) nanostructures exactly play main role for Na^+ ions insertions inside the Mn_2O_3 through Faraday reduction reaction mechanism. Conversely, both of these electrons come back to the ITO through oxidation reaction (in anodic potential scan 0V to 1V); as a result the enhancement of the oxidation current is observed in the same sample. Therefore overall enhancement pseudocapactive current (through faradaic red-ox reaction) of the Mn_2O_3-Au sample compared to pristine Mn_2O_3 is ascribed. So, faradic red-ox reaction which occurs in the Mn_2O_3-Au sample can be proposed and modified as below.

$$Mn_2O_3 + (x+y)Na^+ + (xe^-_{ITO} + ye^-_{Au}) \leftrightarrow Mn_2O_3[(x+y)Na] \qquad (10)$$

Scan rate dependent (0.02 to 1 V/s) CVs of sample Mn_2O_3-Au is shown in Fig. 11c. The shape of the CV curves is identical at all scan rates. These curves also indicate the fast ions diffusion inside the electrode material which induces the enhancement of charge storage capacity through faradic process [37].

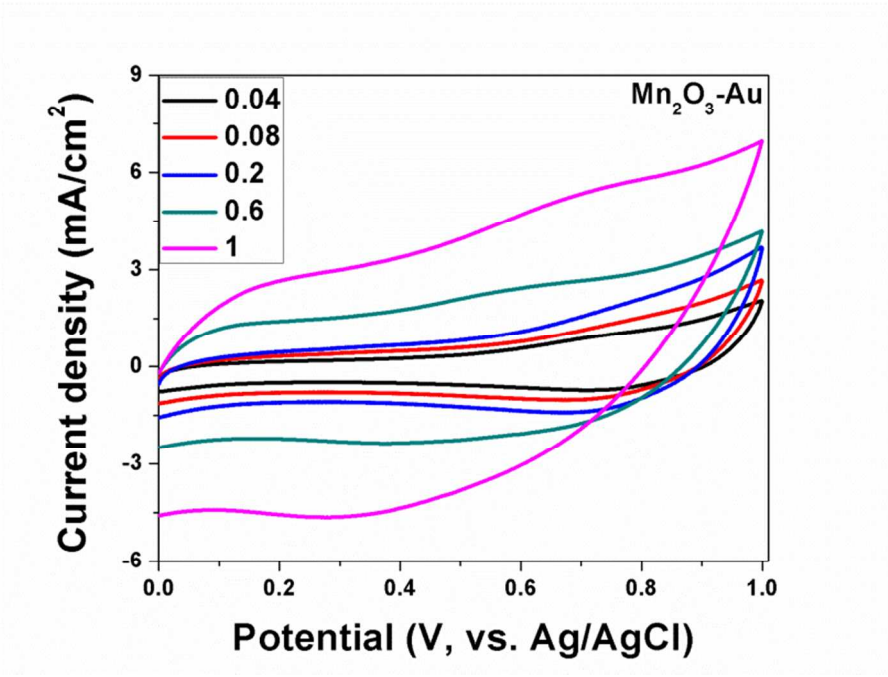

Fig. 11c: CV curves of Mn_2O_3-Au sample at different scan rate.

Conclusions

In summary, we have discussed the one step novel co-electrodeposition technique for the fabrication of Mn_2O_3-Au composite material. The excellent performance of Mn_2O_3-Au electrode can be ascribed to the following reasons: (1) Urchin like gold nanostructure embedded in Mn_2O_3 increases the effective surface area as well as efficient ion intercalation/de-intercalation which attribute to improved charge storage capability of the composite sample compared to pristine Mn_2O_3; 2) the highly conducting metal nanoparticles provides an effective pathway for charge transport; and (3) the binder-free device fabrication enables a low interfacial resistance and fast electrochemical reaction rate. Moreover, frequency response analysis of Mn_2O_3-Au sample confirms also superior charge storage property of the sample which can be used as electrode material for supercapacitor application.

Acknowledgement

Authors would like to thank to Mr. Sumit Majumder, research fellow of Jadavpur University, India for SEM measurements of the samples.

Author's contribution

† These authors have equal contribution to this work.

References:

[1] P. C. Chen, G. Shen, S. Sukcharoenchoke and C. Zhou, *Appl. Phys. Lett.,* 2009, **94**, 043113-043115.

[2] P. J. King, T. M. Higgins, S. De, N. Nicoloso and J. N. Coleman, *ACS Nano*, 2012, **6**, 1732−1741.

[3] S. W. Lee, B. M. Gallant, H. R. Byon, P. T. Hammond and Y. Shao-Horn, *Energy Environ. Sci.*, 2011, **4**, 1972−1985.

[4] S. Park, I. Nam, G. P. Kim, J. W. Han and J. Yi, *ACS Appl. Mater. Interfaces,* 2013, **5**, 9908−9912.

[5] Y. Zhu et al., *SCIENCE*, 2011, **332**, 1537-1541

[6] Q. Cheng, J. Tang, J. Ma, H. Zhang, N. Shinya and L. C. Qin, *CARBON*, 2011, **49**, 2917–2925.

[7] S. K. Jana, V. P. Rao and S. Banerjee, *Chemical Physics Letters*, 2014, **593**, 160–164.

[8] C. D. Lokhande, D. P. Dubal and O. S. Joo, *Current Applied Physics*, 2011, **11**, 255-270.

[9] A. De and P. Sen, *Electrochim. Acta*, 2010, **55**, 4677-4684.

[10] T. Brezesinski, J. Wang, S. H. Tolbert and B. Dunn, *Nature Mater.*, 2010, **9**, 146-151.

[11] A. S. Arico, et al., *Nature Mater.*, 2005, **4**, 366-377.

[12] M. Winter and R. J. Brodd, *Chem. Rev.*, 2004,**104**, 4245-4269.

[13] Y. B. He, G. R. Li, Z. L. Wang, C.Y. Su and Y. X. Tong, *Energy Environ. Sci.*, 2011, **4**, 1288−1292.

[14] R. K. Sharma, A. Karakoti, S. Seal and L. Zhai, *J. Power Sources*, 2010, **195**, 1256–1262.

[15] L. Chen, L. J. Sun, F. Luan, Y. Liang, Y. Li and X. X. Liu, *J. Power Sources,* 2010, **195**, 3742–3747.

[16] G. Yu, L. Hu, N. Liu, H. Wang, M. Vosgueritchian, Y. Yang, Y. Cui and Z. Bao, *Nano Lett.*, 2011, **11**, 4438–4442.

[17] Q. Li, X. F. Lu, H. Xu, Y. X. Tong and R. L. Gao, *ACS Appl. Mater. Interfaces,* 2014, ***6***, 2726–2733,

[18] R. Liu, J. Duay and S. B. Lee, ACS Nano, 2011, **5**, 5608−5619.

[19] Park, S.; Nam, I.; Kim, G. P.; Han, J. W.; and Yi, J., *ACS Appl. Mater. Interfaces*, 2013, **5**, 9908−9912.

[20] J. P. Petitpierre, C. Comninellis and E. Plattner, *Electrochim. Acta*, 1990, **35**, 281-287.

[21] S. K. Jana, T. Majumder and S. Banerjee, *J. Electroanalytical Chemistry*, 2014, **727**, 99–103.

[22] A. Ramírez, P. Hillebrand, D. Stellmach, M. M. May, P. Bogdanoff and S. Fiechter, *J. Phys. Chem. C*, 2014, **118**, 14073−14081.

[23] S. Zhang, K. J. T. Livi, A. C. Gaillot, A. T. Stone and D. R. Veblen, *American Mineralogist*, 2010, **95**, 1741–1746.

[24] G. H. Du, Z. Y. Yuan and G. V. Tendeloo, *Applied Physics Letters*, 2005, **86**, 063113-3.

[25] J. Duay, S. A. Sherril, Z. Gui, E. Gillette and S. B. Lee, *ACS Nano*, 2013, **7**, 1200-1214.

[26] T. Reidl, T. Gemming and K. Wetzig, *Ultramicroscopy*, 2006, **106**, 284-291.

[27] D. H. Pearson, C. C. Ahn and B. Fultz, *Phys. Rev. B*, 1993, **47**, 8471-8478.

[28] X. Lu, Y. Zeng, M. Yu, T. Zhai, C. Liang, S. Xie, M. S. Balogun and Y. Tong, *Adv. Mater.* 2014, **26**, 3148–3155.

[29] X. Lu, G. Wang, T. Zhai, M. Yu, J. Gan, Y. Tong and Y. Li, Nano Lett., 2012, **12**, 1690−1696.

[30] V. G. Bhide and R. V. Damle, *Physica*, 1960, **26**, 33-42.

[31] J. Gamby, P. L. Taberna, P. Simon, J. F. Fauvarque and M. Chesneau, *J. Power Sources*, 2001**, 101**, 109-116.

[32] P. L. Taberna, C. Portet and P. Simon, *App. Phys. A*, 2006, **82**, 639-646.

[33] K. Sheng, Y. Sun, C. Li, W. Yuan and G. Shi, *Scientific Reports*, 2012, **2**, 1-5.

[34] P. L. Taberna, P. Simon and J. F. Fauvarque, *J. Electrochem. Soc.*, 2003, **148**, A292-A300.

[35] C. Portet, P. L. Taberna, P. Simon, E. Flahaut and C. L. Robert, *Electrochimica Acta*, 2005, **50**, 4174–4181.

[36] P. Simon and Y. Gogotsi, *Nature materials*, 2008, **7**, 845-854.

[37] P. C. Chen, G. Shen, Y. Shi, H. Chen and C. Zhou, *ACS Nano*, 2010, **4**, 4403-4411.

Graphical abstract